

# An investigation of precipitation strengthened Inconel 718 superalloy after triode plasma nitriding

Tao, Xiao; Kavanagh, John; Li, Xiaoying; Dong, Hanshan; Matthews, Allan; Leyland, Adrian

DOI:

[10.1016/j.surfcoat.2022.128401](https://doi.org/10.1016/j.surfcoat.2022.128401)

License:

Creative Commons: Attribution-NonCommercial-NoDerivs (CC BY-NC-ND)

*Document Version*

Publisher's PDF, also known as Version of record

*Citation for published version (Harvard):*

Tao, X, Kavanagh, J, Li, X, Dong, H, Matthews, A & Leyland, A 2022, 'An investigation of precipitation strengthened Inconel 718 superalloy after triode plasma nitriding', *Surface and Coatings Technology*, vol. 442, 128401. <https://doi.org/10.1016/j.surfcoat.2022.128401>

[Link to publication on Research at Birmingham portal](#)

## General rights

Unless a licence is specified above, all rights (including copyright and moral rights) in this document are retained by the authors and/or the copyright holders. The express permission of the copyright holder must be obtained for any use of this material other than for purposes permitted by law.

- Users may freely distribute the URL that is used to identify this publication.
- Users may download and/or print one copy of the publication from the University of Birmingham research portal for the purpose of private study or non-commercial research.
- User may use extracts from the document in line with the concept of 'fair dealing' under the Copyright, Designs and Patents Act 1988 (?)
- Users may not further distribute the material nor use it for the purposes of commercial gain.

Where a licence is displayed above, please note the terms and conditions of the licence govern your use of this document.

When citing, please reference the published version.

## Take down policy

While the University of Birmingham exercises care and attention in making items available there are rare occasions when an item has been uploaded in error or has been deemed to be commercially or otherwise sensitive.

If you believe that this is the case for this document, please contact [UBIRA@lists.bham.ac.uk](mailto:UBIRA@lists.bham.ac.uk) providing details and we will remove access to the work immediately and investigate.



# An investigation of precipitation strengthened Inconel 718 superalloy after triode plasma nitriding

Xiao Tao<sup>a,b,\*</sup>, John Kavanagh<sup>b,d</sup>, Xiaoying Li<sup>a</sup>, Hanshan Dong<sup>a</sup>, Allan Matthews<sup>c</sup>, Adrian Leyland<sup>b</sup>

<sup>a</sup> School of Metallurgy and Materials, University of Birmingham, Birmingham B15 2TT, UK

<sup>b</sup> Department of Material Science and Engineering, University of Sheffield, Sheffield S1 3JD, UK

<sup>c</sup> School of Materials, The University of Manchester, Manchester M13 9PL, UK

<sup>d</sup> Department of Chemistry, University of Southampton, Southampton SO17 1BJ, UK

## ARTICLE INFO

### Keywords:

Expanded austenite

Nitriding

Ni-based superalloys

Transmission electron microscopy (TEM)

Precipitation

## ABSTRACT

In this study, we investigated the microstructural evolution, surface hardening and general corrosion properties of a precipitation-strengthened Inconel 718 Ni-superalloy after triode-plasma nitriding (TPN) at low treatment temperatures of 400–450 °C (i.e. thermodynamic paraequilibrium conditions) and a high treatment temperature of 700 °C. At low treatment temperatures, apart from the formation of nitrogen-expanded austenite ( $\gamma_N$ ) from the high-Cr  $\gamma$  matrix, the pre-existing  $\gamma'$  and  $\gamma''$  intermetallic nano-precipitates appear to exhibit different nitriding responses. The spheroidal N-modified  $\gamma'$  (or  $\gamma'_N$ ) precipitates were 'slightly-expanded', leading to slightly shifted XRD peaks, i.e. 2-theta angles of  $\sim 0.2^\circ$  from  $\gamma_{\text{substrate}}(111)$  and  $\sim 0.5^\circ$  from  $\gamma_{\text{substrate}}(200)$ . In contrast, N-modified  $\gamma''$  (or  $\gamma''_N$ ) could experience substantial lattice expansion close to that of the  $\gamma_N$  matrix. With increasing treatment temperature, nitride formation started as additional nano-sized precipitates (e.g.  $\sim 3$ –6 nm diameter as observed at 450 °C) and grew into laths (e.g.  $\sim 5$ –10 nm thick and  $\sim 15$ –30 nm wide as observed at 700 °C).

Without changing core microstructure/properties, surface nitrogen modification and hardening were obtained on alloy 718 after TPN (e.g. from  $\sim 486$  HV<sub>0.025</sub> to  $\sim 1212$  HV<sub>0.025</sub> after TPN at 400 °C). No degradation of corrosion performance was observed for the nitrogen-supersaturated surface after TPN at 400 °C. However, the 450 °C TPN-treated surface showed a slightly increased current density in the anodic region, which can be associated with early-stage nitride formation. The significantly deteriorated corrosion performance after TPN treatment at 700 °C is due to pronounced nitride formation and segregation of substitutional alloying elements.

## 1. Introduction

Plasma nitriding has been established as a successful surface engineering method to modify metal-alloy surfaces with nitrogen and enhance materials' tribological performance. When treated at low temperatures, a hard interstitially-supersaturated layer – known as nitrogen-expanded austenite ( $\gamma_N$ ) [1–4] or S phase [5–8] – can be formed on the surface of austenitic Fe-Cr, Ni-Cr and Co-Cr alloys, that significantly improves wear behaviour without deteriorating (and sometimes even improving) corrosion performance. Nitriding at elevated temperature, e.g. above  $\sim 450$  °C for austenitic stainless steels (ASSs), generally leads to much thicker nitrogen-modified surface layers owing to higher N diffusivity, but is often accompanied by deteriorated corrosion performance owing to local depletion of Cr after the extensive formation of

Cr-nitride precipitates [9].

Inconel 718 is a heat-treatable Ni-based superalloy, originally developed by the International Nickel Company [10] in the late 1950s to provide good mechanical properties at elevated temperatures for aerospace gas turbine engines – subsequently gaining popularity also for offshore oil and gas applications (such as subsurface valves) from the  $\sim 1980$ s onwards [11,12], due to its excellent corrosion performance [10,13,14]. In contrast to most ASSs, Inconel 718 is often heat-treated for optimised strength with microstructures that contain nanoscaled distributions of secondary phases, e.g. coherent spheroidal  $\gamma'$ -Ni<sub>3</sub>(Al, Ti, Nb) of an ordered face-centred cubic (FCC) structure (L1<sub>2</sub>) and semi-coherent disc-shaped  $\gamma''$ -Ni<sub>3</sub>(Nb, Ti) of a body-centred tetragonal (BCT) structure (D0<sub>22</sub>) [15–18]. Incoherent  $\delta$ -Ni<sub>3</sub>Nb needles of an ordered orthorhombic structure (D0<sub>a</sub>) can form from  $\gamma''$ , if heated above

\* Corresponding author at: School of Metallurgy and Materials, University of Birmingham, Birmingham B15 2TT, UK.

E-mail address: [x.tao@bham.ac.uk](mailto:x.tao@bham.ac.uk) (X. Tao).

<https://doi.org/10.1016/j.surfcoat.2022.128401>

Available online 27 March 2022

0257-8972/© 2022 The Authors. Published by Elsevier B.V. This is an open access article under the CC BY-NC-ND license (<http://creativecommons.org/licenses/by-nc-nd/4.0/>).

~850 °C or after prolonged ageing at temperatures above ~650 °C, and could reduce material ductility [15–18].

Although such a nanodispersed precipitation approach can increase alloy mechanical strength without gross elemental segregation to the grain boundaries (that might otherwise cause sensitization and intergranular corrosion), it is still an ongoing challenge to enhance the surface wear performance of Inconel 718 without damaging its corrosion properties. Alloy 718 has been investigated after nitriding at ~400–750 °C [19–28], where enhancements in wear [20,21,24,25,28] and erosion-corrosion resistance [23,27] were often reported, owing to nitrogen modification at the treated surfaces. However, the nitriding response of alloy 718 (and, perhaps also, of other Ni-superalloys) is as yet unclear, with uncertainties typically related to i) surface micro-/nano-structural changes with respect to the desired precipitation-strengthening  $\gamma'/\gamma''$  phases, and ii) the influence of microstructural changes on corrosion resistance.

Since the ~18 at.% Cr in FCC- $\gamma$  matrix of ASS could facilitate nitrogen-supersaturation [29,30], the high-Cr FCC- $\gamma$  matrix of alloy 718 (>~20 at.% Cr) would most likely become interstitially supersaturated with nitrogen and show lattice expansion under low-temperature nitriding. The precipitation-strengthening  $\gamma'$  and  $\gamma''$  phases are, however, low-Cr and high-Ni (<~3 at.% Cr and >~75 at.% Ni) regions that contain substantial levels of strong nitride-forming elements other than Cr (i.e. >~5 at.% Ti and >~5 at.% Al for  $\gamma'$ , and >~16 at.% Nb for  $\gamma''$ ) [18]. Given the characteristic XRD peak shifting observed after nitriding at 400 °C in Ref. [31], it would appear that  $\gamma_N$  layers (denoted as “M” in Ref. [31]) could form in both Ni-Ti (at ~4.9 and ~8.5 at.% Ti) and Ni-Nb (at ~2.6 and ~6.6 at.% Nb) binary alloy systems. However, Ni-6Al binary alloy (~12.2 at.% Al) showed no signs of  $\gamma_N$  formation after nitriding at 400 °C [31]. Similarly, polycrystalline Ni<sub>3</sub>Al showed only a ~100 nm thick surface layer after nitriding at 400 °C for 4 h [32]. Pichon et al. [22,32,33] argued that increasing Al content in  $\gamma'$ -Ni<sub>3</sub>(Al, Ti, Nb) reduces nitrogen incorporation at 400 °C, after comparing the nitriding response of  $\gamma'$  with different compositions in several commercial Ni-superalloys. Taking these factors into account, different nitrogen absorption and lattice distortion behaviours between high-Al  $\gamma'$  and high-Nb  $\gamma''$  can be anticipated, under low-temperature nitrogen-diffusion modification.

To investigate the nitriding response – and the processing-microstructure-performance relationships – of alloy 718 under nitrogen supersaturation under paraequilibrium conditions and with nitride formation approaching thermodynamic equilibrium, a systematic study was carried out for Inconel 718 after triode-plasma nitriding at low (400–450 °C, for 4/20 h) and relatively high (700 °C, for 1/2/4 h) treatment temperatures, respectively. While nitrogen diffusion modification occurs at the near-surface, the core microstructure (and the optimised strength) of the alloy should stay “unharmful” after TPN treatment at 400–450 °C, given the low treatment temperature. Referring also to the time-temperature-transformation diagrams for Inconel 718 [16], a higher treatment temperature at 700 °C was specifically chosen to probe the surface nitriding response of this alloy when approaching thermodynamic equilibrium (meaning roughly the upper temperature limit beyond which a significant change in the metallurgical microstructure of the material core would be expected). The nitriding treatment carried out at 700 °C was limited to a maximum of 4 h to avoid  $\delta$ -Ni<sub>3</sub>Nb formation.

## 2. Experimental

Inconel 718 was received in age-hardened condition and prepared into flat sample coupons of 50 mm × 25 mm × 2 mm. Material composition was confirmed using SEM-EDX as shown in Table 1. Sample coupons were mechanically polished to a mirror surface finish (Ra ≤ 0.05  $\mu$ m) using mechanical grinding and polishing, with 6  $\mu$ m and 1  $\mu$ m diamond suspension as the final steps. Samples were ultrasonically cleaned in acetone for 15 min, in isopropanol for 10 min, and then dried

**Table 1**

Chemical composition of Inconel 718, wt%.

	Ni	Fe	Cr	Nb	Mo	Al	Ti	Others
Inconel 718	50.7	Bal.	18.9	5.4	3.5	0.6	1.0	0.2 Co, 0.2 Mn, 0.1 Cu, 0.1 Si, <sup>a</sup> 0.08 C max., <sup>a</sup> 0.015 P max., <sup>a</sup> 0.015 S max., <sup>a</sup> 0.006 B max.

<sup>a</sup> The contents of C, P, S and B are listed according to ASTM B670-07 (2018), while the concentrations for other elements are confirmed under SEM-EDX.

under dry compressed air.

Nitriding treatments were carried out in a modified Tecvac IP70L commercial PVD coating unit, using a triode plasma nitriding (TPN) configuration [3,34,35], with a hot tungsten filament, that is AC electrical-resistance-heated (for generation of thermionic electrons) and simultaneously DC negatively biased (for expelling/accelerating thermionic electrons), as an additional electrode for plasma intensification. This approach provides numerous advantages, such as plasma stabilization at low ( $\leq 200$  V) treatment voltage (for precise control of cathode sheath thickness and ion-energy distribution at the workpiece), avoidance of the need for hydrogen in the treatment gas (due to the high surface sputter yield from intense ion bombardment – that can efficiently remove nascent oxide films) and incidental hydrogen-induced issues (such as hydrogen embrittlement and hydride formation), and the ability – particularly with ferritic/martensitic/duplex steels – to control or eliminate the development of brittle surface nitride layers during treatment [34,35]. TPN treatment was carried out at low treatment temperatures of 400 °C, 425 °C and 450 °C for 4 h and 20 h, respectively (as described in [36,37]). To investigate the high-temperature plasma nitriding behaviour of alloy 718, TPN was also carried out at 700 °C for 1 h, 2 h and 4 h, respectively (as described in [38], which has been adopted previously for sub-beta-transus TPN-treatment of Ti-alloys [39–42]). Sample denotation in this paper is based on treatment temperature and time, as shown in Table 2. For example, alloy 718 after TPN treatment at 400 °C for 20 h is denoted as 400-20.

Prior to TPN treatment, the process chamber was firstly evacuated to a base pressure  $< 2 \times 10^{-3}$  Pa. Plasma sputter cleaning was carried out for 15 min under 2 Pa Ar atmosphere with a workpiece bias of –800 V. The main nitriding parameters were kept the same for all TPN treatments, i.e. working pressure at 0.4 Pa, 7:3 N<sub>2</sub>:Ar gas volume ratio, hot-filament bias at –200 V and workpiece bias also at –200 V. However, in addition to higher thermal radiation from auxiliary heating units, a much greater AC electrical-resistance heating power was applied to the hot filament (to enhance levels of thermionic emission from the filament and thereby intensify plasma ion-bombardment heating of substrates [43]) to reach/maintain a high treatment temperature during TPN treatments at 700 °C, compared to TPN treatments at 400–450 °C.

**Table 2**

Surface nitrogen contents (SEM-EDX) and layer thicknesses determined before etching and after etching for alloy 718 after TPN treatments. Data are presented as mean  $\pm$  standard deviation.

Code	Treatment temperature & time	Surface N content, at.%	Layer thickness, $\mu$ m	
			From BS-SEM	After etching
Untreated	/	/	/	/
400-4	400 °C 4 h	22.3 $\pm$ 1.1	1.8 $\pm$ 0.1	/
400-20	400 °C 20 h	23.4 $\pm$ 1.2	4.2 $\pm$ 0.2	4.0 $\pm$ 0.2
425-4	425 °C 4 h	20.3 $\pm$ 1.5	/	/
425-20	425 °C 20 h	21.6 $\pm$ 1.6	/	/
450-4	450 °C 4 h	20.1 $\pm$ 1.3	3.8 $\pm$ 0.6	/
450-20	450 °C 20 h	21.5 $\pm$ 0.9	7.1 $\pm$ 0.3	7.2 $\pm$ 0.2
700-1	700 °C 1 h	16.2 $\pm$ 0.8	1.1 $\pm$ 0.1	1.2 $\pm$ 0.1
700-4	700 °C 4 h	14.7 $\pm$ 1.2	1.5 $\pm$ 0.2	/

During TPN, the AC electrical currents for the filament resistance heating are typically  $\sim 58$ – $65$  A (for treatments at  $400$ – $450$  °C) and  $70$  A (for treatment at  $700$  °C). After TPN treatment, samples were cooled in vacuum  $<0.1$  Pa to below  $200$  °C before venting, to minimize surface oxidation.

Optical microscopy (OM) was performed using a Nikon Eclipse LV150 with Buehler Omni Met software. Sample cross-sections were prepared and examined under scanning electron microscopy (SEM) after etching in glyceric acid and back-scattered electron microscopy (BS-SEM) before etching, using an FEI Nova NanoSEM 450 instrument. Surface roughness was evaluated by stylus profilometry (Veeco Dektak 150, equipped with a  $12.5$   $\mu\text{m}$  radius diamond tip). A Dimension 3100 atomic force microscope (AFM) was used to show detailed surface morphology. Energy Dispersive X-ray (EDX) spectroscopy was carried out via a Philips XL30S FEG scanning electron microscope equipped with Oxford Instruments INCA EDX system. The beam intensity was calibrated with a cobalt standard. Nitrogen-depth profiles were evaluated via glow discharge optical emission spectroscopy (GDOES) using a Spectruma GDA650HR instrument.

X-ray diffraction (XRD) analysis was performed in Bragg-Brentano geometry using a Bruker D2 PHASER (30 kV, 10 mA; Cu-K $\alpha_{\text{ave}}$  0.1542 nm) and in Seeman-Bohlin geometry at  $2^\circ$  glancing angle (GAXRD) using a PANalytical X'pert<sup>3</sup> instrument (45 kV, 40 mA; monochromated Cu-K $\alpha_1$  0.1541 nm). X-ray attenuation depths on alloy 718 were estimated using AbsorbDX software (95% X-ray signal), being  $\sim 2$ – $5$   $\mu\text{m}$  for conventional Bragg conditions and  $< \sim 1$   $\mu\text{m}$  for GAXRD. Transmission electron microscopy (TEM) samples were extracted cross-sectionally and prepared from the TPN-treated surfaces using an FEI Quanta 200 3D instrument, coupled with a Ga<sup>+</sup> ion beam source. Bright-field (BF) and dark-field (DF) TEM images, and electron diffraction patterns (EDPs), were taken using a Philips EM420 microscope (Tungsten filament, 120 kV), a Jeol 2100 microscope (LaB<sub>6</sub> filament, 200 kV) and an FEI Tecnai F20 microscope (FEG, 200 kV). High-angle annular dark-field (HAADF) imaging and EDX analyses were carried out under scanning TEM (STEM)

mode using an FEI Tecnai F20 microscope (FEG, 200 kV, C2 = 70  $\mu\text{m}$ , nanoprobe 3).

Vickers hardness was measured using a Struers Durascan® 70 hardness tester and averaged from at least 8 random indents across the sample surface. Indentation loads were 0.01, 0.025, 0.05, 0.1, 0.2, 0.3, 0.5, and 1 kg. Indentation dwell time was 15 s. Potentiodynamic polarization was performed in an electrochemical cell with a Saturated Calomel reference electrode (SCE, Hg/HgCl<sub>2</sub> – Sat. KCl) and a platinum counter electrode. A surface area of  $\sim 0.79$  cm<sup>2</sup> was exposed in 3.5 wt% NaCl solution for 3600 s for open circuit potential (OCP) stabilization and then polarised from  $-1$  V to  $+2$  V at a scan rate of 1.67 mV/s. Process monitoring, data collection and analysis were performed using a proprietary Scribner/Solartron CorrWare® software.

### 3. Results and discussion

#### 3.1. Surface morphology, cross-section morphology and layer thickness

Under OM, a microstructure of  $\sim 5$ – $30$   $\mu\text{m}$  equiaxed grains can be seen on the surface of TPN-treated alloy 718 at  $400$ – $450$  °C (Fig. 1a & b), similar to that of TPN-treated ASSs under equivalent treatment conditions – see for example Ref. [37]. The observed topological effects are likely due to a combination of plasma etching (from the intense sputtering of the triode plasma) and a “swelling effect” [44] (from nitrogen interstitial supersaturation). Secondly, while no significant change in surface roughness was measured after TPN treatment at  $400$ – $450$  °C (with  $R_a$  values remaining  $\leq 0.05$   $\mu\text{m}$ ), the surface  $R_a$  value increased to 0.28, 0.24 and 0.32  $\mu\text{m}$  for 700-1, 700-2, and 700-4 treatments, respectively. The apparently rougher surface on  $700$  °C treated samples in Fig. 1c (compared to those treated at  $400$ – $450$  °C in Fig. 1a & b) can be associated with significantly more intense sputtering effects at the higher temperature (due to the additional plasma heating required to reach/maintain high treatment temperature). The high number density of bright spots in Fig. 1c corresponds to sharp asperities, as revealed in

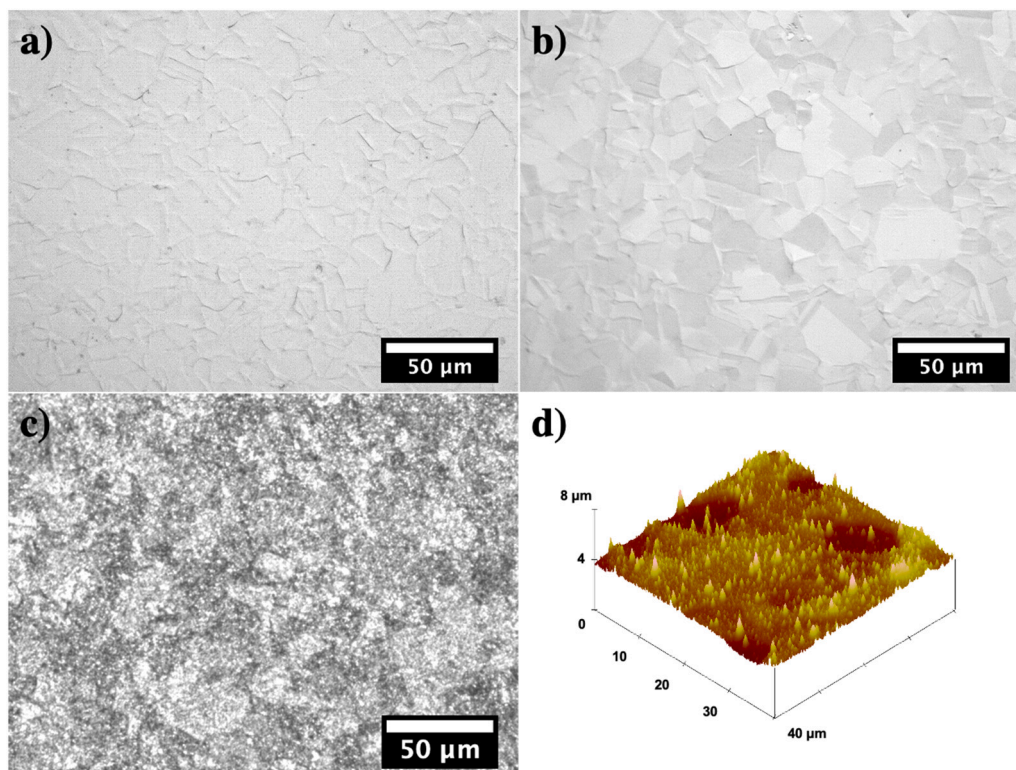


**Fig. 1.** Optical micrographs (top-view) showing the surface of Inconel 718 after TPN a) at  $400$  °C for 20 h, b) at  $450$  °C for 20 h and c) at  $700$  °C for 4 h; d) AFM image showing the surface morphology after TPN at  $700$  °C for 4 h.



Fig. 1d. Additionally, it is worth mentioning that ‘picture frame’ edge sputtering effects were absent from all TPN-treated samples, owing to the low workpiece bias potential applied and the dramatically lowered  $L/\lambda_C$  ratio in triode plasma treatments (where L stands for cathode sheath thickness and  $\lambda_C$  stands for ion collision cross section) [34,43,45].

The prepared sample cross-sections were examined under BS-SEM imaging (see Fig. 2a–f), where a dark layer was observed on all TPN-treated surfaces. The dark appearance in backscattered SEM imaging is owing to high nitrogen absorption in the layer. Treatment layers were then revealed after etching in glyceric acid (see Fig. 2g–i). A uniform treatment layer was seen on 400-20 (Fig. 2g), owing to nitrogen supersaturation (see phase analysis in Section 3.2). A double-layered structure was seen for the treatment layer of 450-20 in Fig. 2h, which could be associated with nitride formation (in the  $\sim 6 \mu\text{m}$  thick topmost layer) and nitrogen supersaturation (for the  $\sim 1 \mu\text{m}$  thick underlying region). A thin surface layer (of only  $\sim 1.2 \mu\text{m}$  thickness) was revealed for 700-1 in Fig. 2i.

Layer thicknesses were measured from both BS-SEM images before etching and SEM images after etching (at 5 random locations, with 5 measurements made in each location) as shown in Table 2. The layer depths measured after etching correlate well to those measured from BS-SEM. In general, treatment layer thickness was found to increase with both treatment time and temperature. The layer thickness was reported to reduce with increasing treatment temperature for Ni superalloys after gaseous nitriding (for a series of Nimonic alloys treated at 400 °C and 440 °C [46]) and after plasma nitriding (for Inconel 600 treated at 400–600 °C, from  $\sim 450$  °C upwards [47]). The proportional drop in layer depth for plasma nitrided Inconel 600 was attributed to an increasingly thicker surface oxide scale at higher treatment temperatures (and longer times), that was believed to block nitrogen inward diffusion [47]. Noticeably, oxide scale was not observed in this study on all TPN-treated surfaces (e.g. see Fig. 2), probably owing to a much

lower level of residual oxygen (comparing the base vacuum level  $< 2 \times 10^{-3}$  Pa in this study and  $< 7$  Pa in Ref. [47]), intense ion bombardment during TPN, and the vacuum cooling step, post-treatment.

Amongst the 4 h TPN-treated samples, 700-4 appears to have the shallowest case depth at  $\sim 1.5 \mu\text{m}$  (Table 2). However, despite the main treatment parameters being kept the same, bombardment effects – as also evidenced from the difference in surface roughness and morphology (Fig. 1) – were much more intense (primarily for substrate heating purposes) for the TPN treatments at 700 °C in this study, compared to the TPN treatments at 400–450 °C. Strong plasma sputter-removal effects (as observed for Ti alloys with pre-deposited PVD coatings after TPN treatment – see Ref. [48]) are believed to contribute to the reduced layer thickness at 700 °C. Additionally, Fig. 2 did not resolve an underlying N diffusion zone for those treated at 700 °C (see GDOES, Fig. 9), in which case the total nitrogen treatment depth could be deeper than the layer thicknesses measured from SEM.

### 3.2. Microstructural evolution

#### 3.2.1. The unmodified material core

Firstly,  $\gamma'/\gamma''$  precipitates share similar lattice parameters to the  $\gamma$ -FCC matrix and cannot be resolved under XRD (as labelled in Fig. 3). Spheroidal  $\gamma'$  ( $\sim 5$ –20 nm diameter) and narrow  $\gamma''$  platelets were revealed under TEM in Fig. 4. Both Fig. 4a and c were respectively taken in the unmodified core ( $> \sim 5 \mu\text{m}$  deep) on 700-1 and 400-20, showing the fine  $\gamma'/\gamma''$  precipitation morphology retained in the material core after TPN treatment. Apart from large FCC diffraction spots (where  $\gamma'/\gamma''$  diffraction maxima overlap), superlattice diffraction spots were observed (as indicated by arrows in Fig. 4b & d), corresponding to  $\gamma'$  and  $\gamma''$  [49,50]. The superlattice diffraction spot encircled in Fig. 4b corresponds to  $\gamma''$  only. In addition, a peak at  $\sim 34.8^\circ$  could be seen in both Fig. 3a & b for alloy 718 before and after TPN, which is attributable to

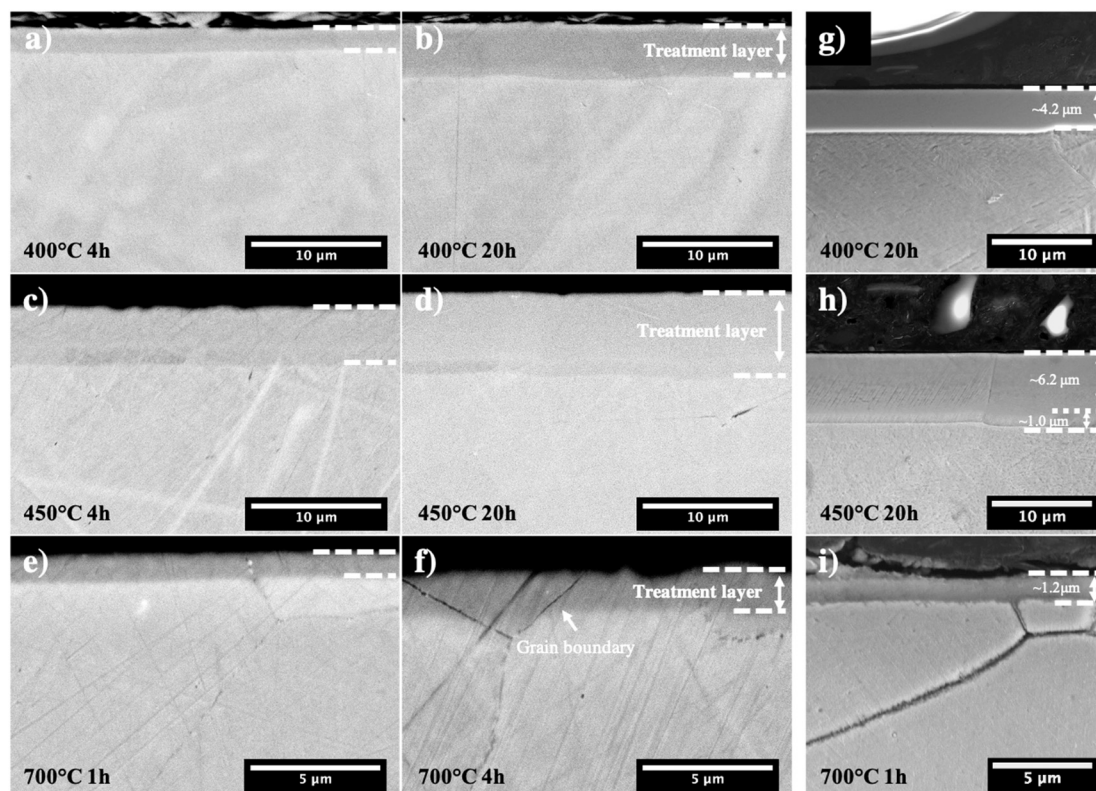


Fig. 2. BS-SEM images for Inconel 718 cross-sections (without etching) after TPN treatment at a) 400 °C for 4 h, b) 400 °C for 20 h, c) 450 °C for 4 h, d) 450 °C for 20 h, e) 700 °C for 1 h, and f) at 700 °C for 4 h; and SEM images for Inconel 718 cross-sections (after etching) after TPN treatment at g) 400 °C for 20 h, h) 450 °C for 20 h, and i) 700 °C for 1 h. Note the scale bar is 5  $\mu\text{m}$  in Fig. 2e & f & i.

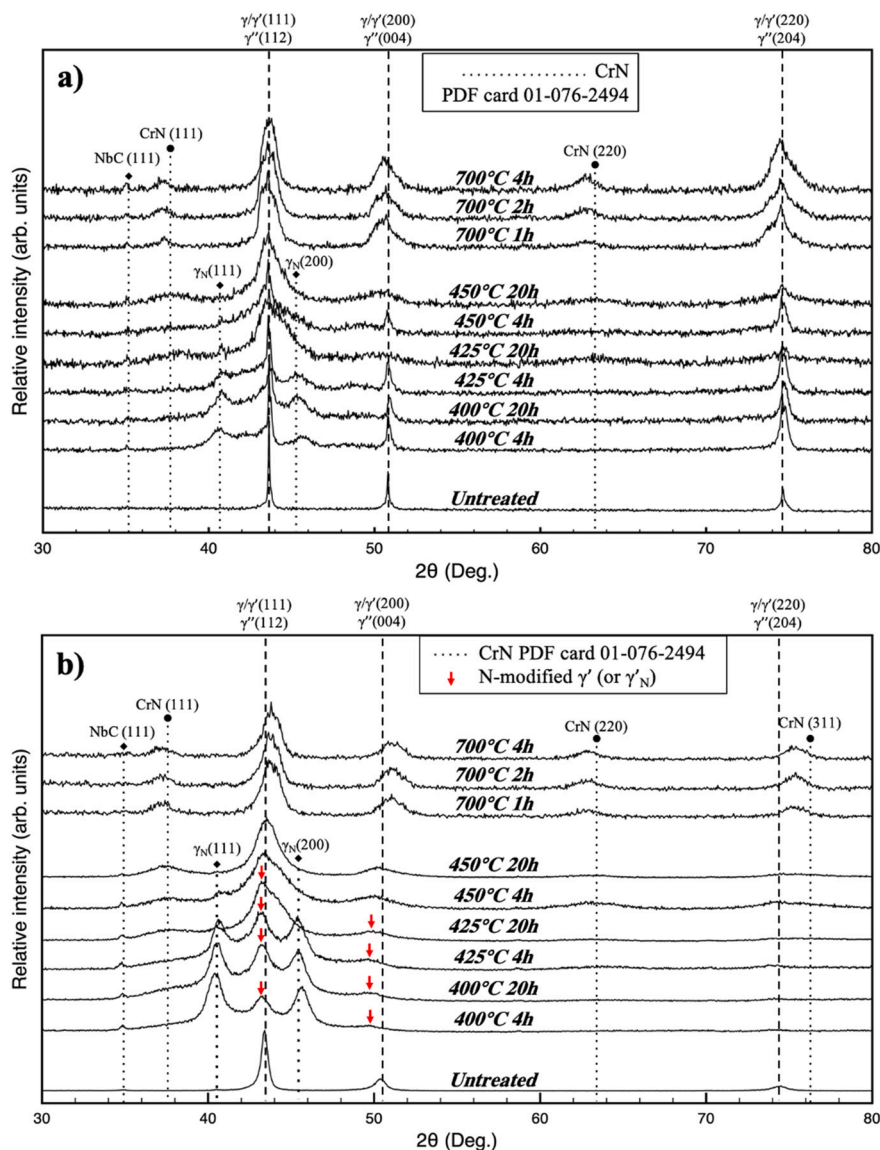


Fig. 3. a) XRD and b) GAXRD profiles of samples before and after TPN treatments.

NbC(111). Note that the XRD profiles in Fig. 3 were normalised and plotted in one figure for comparison purposes. Minor XRD peaks – although not obvious in Fig. 3 – can be observed for the untreated alloy 718 (see Fig. A1, Appendix A), indicating that NbC exists before (rather than induced from) TPN treatments.

### 3.2.2. Nitrogen supersaturation

At treatment temperatures of 400–450 °C, XRD and GAXRD profiles (Fig. 3) indicate the formation of  $\gamma_N$  on Inconel 718 after TPN treatment. Similar to ASSs, the peak shift of  $\gamma(200)$  to  $\gamma_N(200)$  is always more than that of  $\gamma(111)$  to  $\gamma_N(111)$  for alloy 718 under nitrogen interstitial supersaturation, corresponding to the systematic anisotropic expansion of the FCC lattice (with stiffer, close-packed (111) planes tending to expand less than the relatively compliant (200) planes). Using (111) and (200) XRD peaks from Fig. 3b, the lattice parameters of  $\gamma_N$  can be estimated as being  $a_{\gamma_N(111)} \sim 0.38$  nm and  $a_{\gamma_N(200)} \sim 0.40$  nm, respectively. Saturated lattice expansion was reached quickly for alloy 718 after 4 h of TPN treatment at 400 °C, which agrees with the quick expansion saturation for a high-Ni austenitic stainless steel after TPN treatment (e.g. alloy RA330, compared to AISI304 and high-Mn alloy AG17 [37]). Besides, similar to that revealed in an ion implantation

study [51], a commercially pure Ni showed no observable changes in XRD after TPN treatment at 450 °C (Fig. A2, Appendix A), which indicates the importance of nitride-forming elements for nitrogen uptake in Ni-alloys.

Apart from  $\gamma_N$  peaks, samples treated at low temperatures of 400 °C and 425 °C always exhibit peaks at  $\sim 43.2^\circ$  and at  $\sim 49.7^\circ$  (as indicated by the red arrows in Fig. 3b), which are located near, yet appear to be slightly shifted from, substrate  $\gamma/\gamma'/\gamma''(111)$  and  $\gamma/\gamma'/\gamma''(200)$  positions, respectively. Considering the shallow X-ray attenuation depth (i.e.  $< 1$   $\mu\text{m}$ ) under GAXRD, these “slightly-shifted” peaks at  $\sim 43.2^\circ$  and  $\sim 49.7^\circ$  originate from the treatment layer (rather than the substrate). The coexistence with  $\gamma_N$  of such a “slightly-expanded” phase on TPN-treated alloy 718 has never been reported for  $\gamma_N$  layers synthesised on ASSs (e.g. on AISI 304, high-Mn alloy AG17 and ultra-high Ni RA330) after equivalent TPN treatments [37,52,53].

Under TEM, a spheroidal phase of  $\sim 5$ – $20$  nm diameter was revealed for the TPN-treated surface on 400-20, as indicated by arrows in Fig. 5a. Similar to the two sets of XRD peaks for the 400-20 surface in Fig. 3b (i.e.  $\gamma_N$  and the “slightly-shifted” peaks), EDPs in Fig. 5c & d show two sets of diffraction spots. Corresponding to the outer diffraction spot in Fig. 5c, a spheroidal-shaped phase was revealed under DF-TEM image in Fig. 5b,

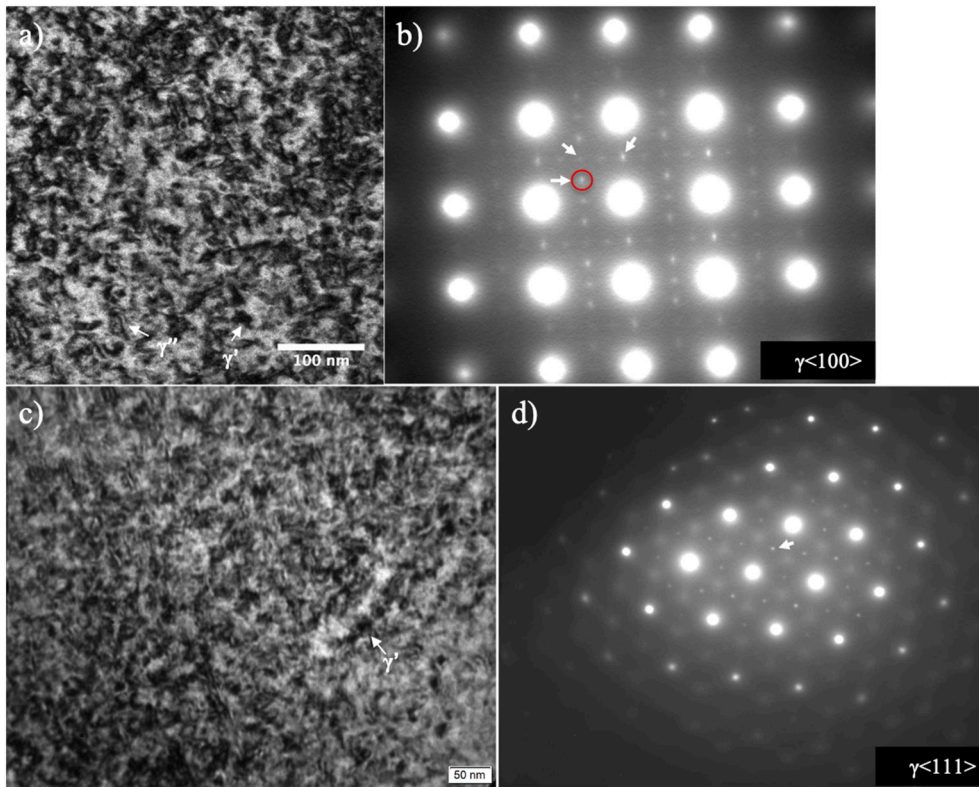


Fig. 4. BF-TEM images and corresponding EDPs for the unmodified core of alloy 718 treated at a, b) 700 °C for 1 h and c, d) at 400 °C for 20 h, showing  $\gamma'/\gamma''$  nano-precipitation morphology. Superlattice reflections are indicated by arrows in Fig. 4b & d.

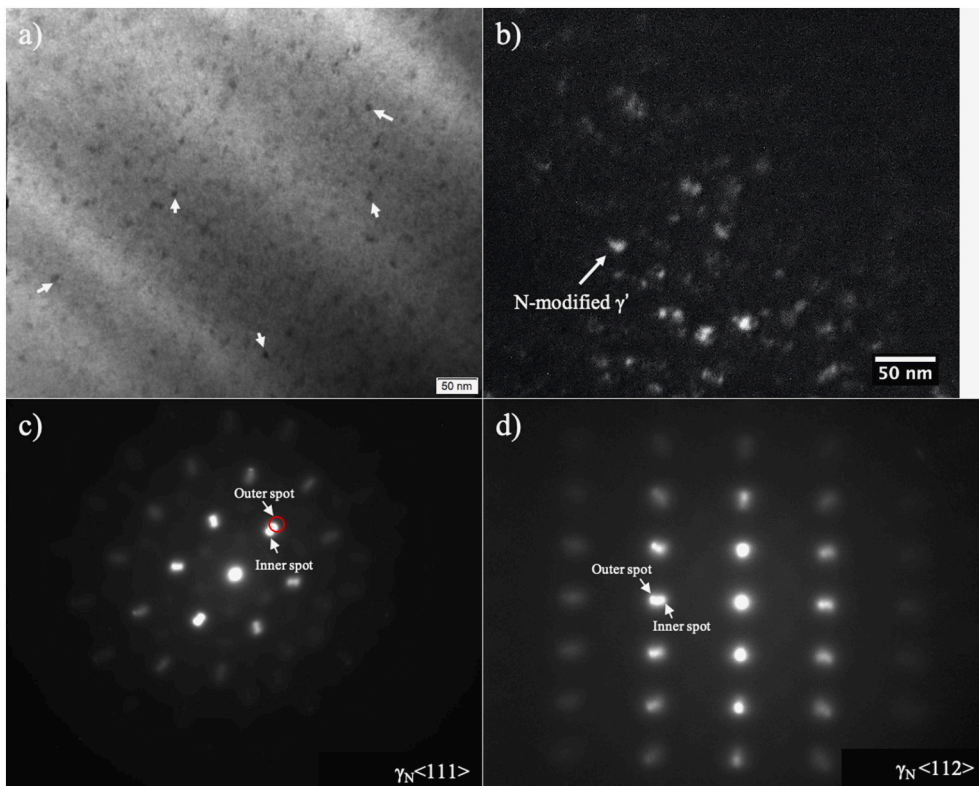


Fig. 5. a) BF-TEM image, b) DF-TEM image (acquired using reflections encircled in Fig. 5c), and c, d) corresponding EDPs for the treatment layer (taken at depth < 1  $\mu\text{m}$ ) on alloy 718 after TPN treatment at 400 °C for 20 h.



which can be identified as N-modified  $\gamma'$  (or  $\gamma'_N$ ). It is thus believed that  $\gamma'_N$  gives rise to the “slightly-shifted” XRD peaks in Fig. 3b. Chollet et al. [22] and Pichon et al. [32,33] also reported similar slightly-expanded  $\text{Ni}_3\text{Al}$ -type  $\gamma'$  phase (owing to its high Al-content at  $\sim 15$  at.%) in another Ni-superalloy, alloy MC2, with “almost no N” after nitriding at  $400^\circ\text{C}$ . The slight lattice expansion of  $\gamma'_N$  in alloy 718 could be associated with a lower level of nitrogen absorption with (locally) high Al content.

Referring to the GAXRD profile for 400-20 in Fig. 3b, the inner electron diffraction spots in Fig. 5c & d are attributable to the nitrogen supersaturated matrix,  $\gamma_N$ . The diffraction distance ratio for the outer and inner diffraction spots in Fig. 5c & d is measured as being  $\sim 1.09$ – $1.10$ , which is comparable to  $\sim 1.06$  for the lattice parameter ratio of  $\gamma_N$  over  $\gamma'_N$ , estimated using (111) peaks from Fig. 3b. The slight deviation in the ratio values could come from the ‘distorted’ FCC lattice for bulk material under XRD and stress relaxation during TEM sample thinning (as previously demonstrated in Ref. [37]). For example, compared to the anisotropic lattice expansion under XRD,  $\gamma_N$  appears almost isotropic in EDP under TEM (Fig. 5d), i.e.  $a_{\gamma_N(111)} = 0.398$  nm and  $a_{\gamma_N(200)} = 0.404$  nm. In addition, lenticular  $\gamma''$  precipitates were not observed on 400-20 under DF-TEM in Fig. 5b, in which case  $\gamma''_N$  and  $\gamma_N$  matrix most likely share a similar lattice expansion, contributing to the inner diffraction spots in Fig. 5c & d. Consistently, no other ‘new’ XRD peaks were seen in Fig. 3, in which case the peak for N-modified  $\gamma''$  (or  $\gamma''_N$ ) most likely overlaps with the broad  $\gamma_N$  peaks. The  $\gamma''_N$  could have an expanded BCT structure, that is semi-coherent to the expanded  $\gamma_N$  matrix. In these regards, the inner and outer diffraction spots in Fig. 5c & d could be identified as corresponding to  $\gamma_N$  (plus  $\gamma''_N$ ) and  $\gamma'_N$ , respectively.

### 3.2.3. Nitride formation at elevated treatment temperature

With increasing treatment temperature (and/or time) from bottom to

top in Fig. 3a & b, both the  $\gamma_N(111)$  peak at  $\sim 40.5^\circ$  and the  $\gamma_N(200)$  peak at  $\sim 45.6^\circ$  diminish above  $\sim 425^\circ\text{C}$ , while a new peak emerges at  $\sim 37.5^\circ$  and becomes more intense (approaching thermodynamic equilibrium), that could be indexed as CrN(111). A small  $\gamma_N(111)$  peak could still be seen even after CrN formation in samples 425-20, 450-4, and 450-20 under GAXRD (Fig. 3b), hinting at residual  $\gamma_N$  in the treatment layer (note the  $< 1\ \mu\text{m}$  X-ray attenuation depth). At  $700^\circ\text{C}$ , no  $\gamma_N$  peaks were observed, but CrN peaks can be identified at  $\sim 37.2^\circ$  and  $\sim 62.8^\circ$  (as indicated in Fig. 3). In addition, the peak for  $\gamma'_N$  at  $\sim 43.2^\circ$  appears to shift back to its original position at  $\sim 43.5^\circ$  as the treatment temperature increases (Fig. 3b). Additionally, the  $\gamma_N$  (plus  $\gamma''_N$ ) peak apparently diminishes with increasing treatment temperature/time. In these regards, CrN appears to form at the expense of all three ‘nitrogen-expanded’ phases:  $\gamma_N$ ,  $\gamma'_N$  and  $\gamma''_N$ .

Similar to Fig. 5a, the BF-TEM image in Fig. 6a for the treatment layer on 450-20 also shows  $\sim 5$ – $20$  nm diameter spheroidal precipitates (as indicated by arrows), which could be identified as  $\gamma'$  (or residual  $\gamma'_N$ ). However, when compared to Fig. 5a for 400-20, Fig. 6a for 450-20 appears rather “noisy” with many additional small “dots”. Corresponding to the inner spot encircled in Fig. 6d, “dotted” regions with diameters ranging from  $\sim 3$  to  $6$  nm were revealed on 450-20 under DF-TEM imaging in Fig. 6b, which are attributable to nitride formation. The corresponding EDPs for 450-20 in Fig. 6c & d also show two sets of diffraction spots, but in clear separation from each other (compared to the adjacent diffraction spots for 400-20 in Fig. 5c & d). Diffraction distance ratios for the outer and inner diffraction spots in Fig. 6c & d are measured as being  $\sim 1.152$ , which agrees very well with the lattice parameter ratio of CrN over unmodified  $\gamma$  at  $\sim 1.157$ , estimated from the CrN(111) peak at  $\sim 37.4^\circ$  and the  $\gamma(111)$  peak at  $\sim 43.5^\circ$  for 450-20 from Fig. 3b. The nitrides formed follow a cube-on-cube orientation relationship to the  $\gamma$  matrix:  $\{111\}_{\text{nitride}} // \{111\}_\gamma$  and  $\{110\}_{\text{nitride}} // \{110\}_\gamma$ . Referring to the shallow CrN XRD peaks for 450-20 in Fig. 3b (compared

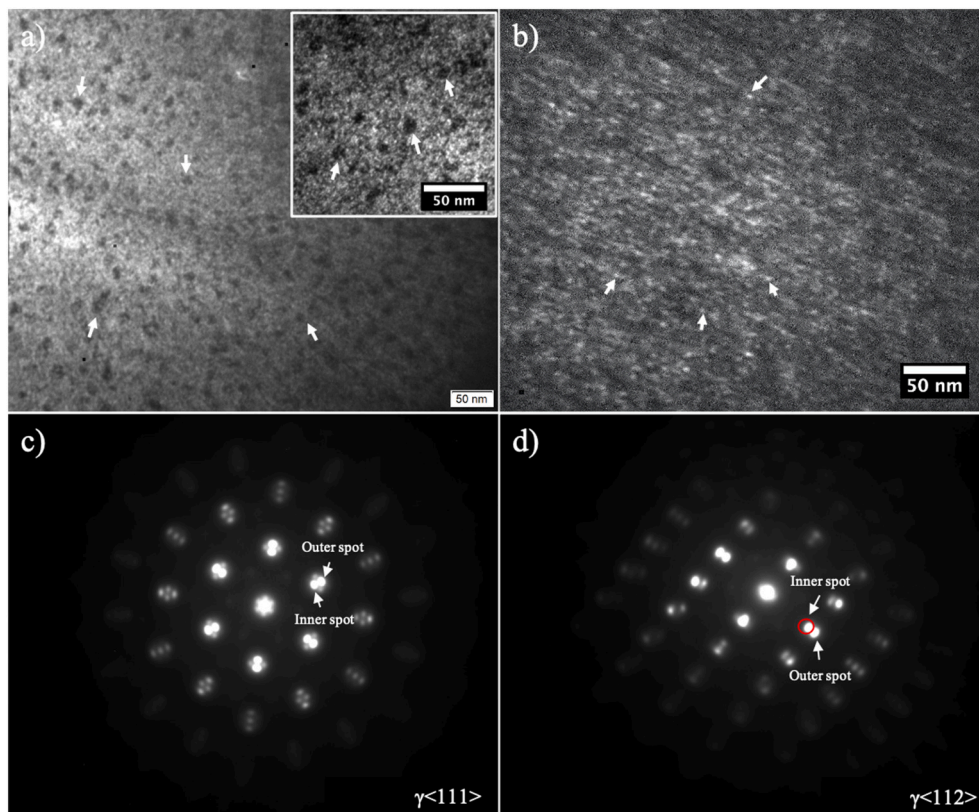


**Fig. 6.** a) BF-TEM image (inset: BF-TEM image at a higher magnification), b) DF-TEM image (acquired using reflections encircled in Fig. 6d), and c) corresponding EDPs for the topmost treatment layer (taken at depth  $< 1\ \mu\text{m}$ ) on alloy 718 after TPN treatment at  $450^\circ\text{C}$  for 20 h.



to the sharp ones for 700-1, the treated surface of 450-20 is in an intermediate paraequilibrium state with nitride formation being at a very early stage.

In contrast to the predominantly “dotted” precipitation morphology on 450-20, nitride precipitates appear to coalesce and form a “woven” morphology, as revealed for the topmost layer on 700-1 under STEM-HAADF imaging, as shown in Fig. 7a. Nitride precipitates are thought to nucleate, grow (and gradually coalesce) along the semi-coherent interfaces between  $\gamma''$  and  $\gamma$  matrix within the austenite grains. The nitride laths in Fig. 7a, which appear black under STEM-HAADF (Z-contrast) owing to low mean atomic weight at high nitrogen content, show thicknesses ranging from  $\sim 5$  to 10 nm and widths ranging from  $\sim 15$  to 30 nm. In the corresponding EDPs in Fig. 7b & c, the diffraction distance ratio for the outer and inner spots is measured as being  $\sim 1.171$ , which agrees very well with the lattice parameter ratio between CrN and  $\gamma$  at 1.169, the latter being estimated using the CrN(111) peak at  $\sim 34.2^\circ$  and the  $\gamma(111)$  peak at  $\sim 43.8^\circ$ , for 700-1, from Fig. 3b. The satellite diffraction spots in Fig. 7b & c could be associated to double diffraction and the modulated structure [54], with nitride nano-precipitates distributed preferentially along the  $\gamma''$  laths.

### 3.2.4. Ti-/Nb-containing CrN

Since TiN and (metastable) AlN share a very similar FCC crystallographic structure to CrN, the nitride identified in TPN-treated Ni-superalloys could comprise CrN, TiN and AlN (as also argued by Eliason et al. [46] for gas-nitrided Ni-alloys). Nevertheless, the slightly shifted XRD peak positions for the “CrN” peaks at 700 °C in Fig. 3 hints that a fraction of the Cr atoms in CrN could also be substituted with Ti, Nb and/or Al atoms, i.e. (Cr, Ti, Al, Nb) N. It is rather difficult to evaluate the precise chemical composition for these small nitride precipitates with  $\sim 3$ –6 nm diameter on 450-20 (bearing in mind their 3D distribution in a  $\sim 100$  nm thick TEM sample).

However, the STEM-EDX analyses carried out for the rather large nitride(s) on 700-1 present sharp contrast with valuable information in Fig. 8. The dark nitride region highlighted in Region I in Fig. 8a appears to have low concentrations of Ni and Fe, but high concentrations of Cr, Nb, Ti and N (Fig. 8b–i), which suggests Ti-/Nb-containing CrN on 700-1. The bright lath highlighted in Region II in Fig. 8a shows high-Ni (Fig. 8b), high-Fe (Fig. 8c), low-Cr (Fig. 8d) and low-N (Fig. 8i), presumably being the  $\gamma$  matrix. EDX maps for Mo (Fig. 8f) and Al (Fig. 8h) show low signal contrast, suggesting a rather homogenous elemental distribution. While Cr and N maps almost superimpose with each other (Fig. 8d & i), the distribution of Nb and Ti (Fig. 8e & g) does not always comply with that of Cr and N (Fig. 8d & i), which can be attributed to residual  $\gamma'/\gamma''$  regions after partial segregation of Ti and Nb to nitrides and the variation of Ti and Nb content in (Cr, Ti, Nb)N.

Additionally, it is worth mentioning that the phase constituents and their precise chemical composition on 700-1 would still require further investigations (e.g. using advanced Atom Probe Tomography, APT – as

illustrated in Ref. [18]). The low image contrast of Mo and Al seems to be due to their low chemical concentrations (since their Z-contrast should otherwise be high), in which case the precise elemental distributions of Mo and Al are still ambiguous. Similar low-contrast images were observed for other minor alloying elements (most likely owing to their small content in the alloy system), and their EDX maps were not included in Fig. 8.

### 3.2.5. Absence of superlattice reflections

Last but not least, the superlattice diffraction spots – which are “forbidden reflections” in FCC structures (but originate from the ordered structure of  $\gamma'/\gamma''$ ) – were seen from the unmodified cores (as indicated by arrows in Fig. 4b, d), but were absent for the topmost treatment layer on 400-20 (Fig. 5c & d), 450-20 (Fig. 6c & d) and 700-1 (Fig. 7b & c). Upon nitride formation at 450 °C and 700 °C, one may anticipate partial segregation of Nb/Ti/Al from  $\gamma'/\gamma''$  towards nitride(s) at these elevated treatment temperatures (referring to the STEM-EDX analysis in Fig. 8), that destroys the ordered structure of  $\gamma'/\gamma''$  and diminishes superlattice reflections. However, the ordered structure of  $\gamma'/\gamma''$  should be maintained after TPN at the lowest treatment temperature of 400 °C, where the segregation of larger substitutional elements is suppressed.

Nitrogen short-range ordering – and in some cases, long-range ordering (such as an “Fe<sub>4</sub>N-like” phase [55,56]) – has been reported in some FCC- $\gamma_N$  layers synthesised on ASSs at low treatment temperatures around 400 °C, that leads to the observation of forbidden reflections in EDPs for FCC- $\gamma_N$  [37,57,58]. In this regard, strong superlattice reflections were expected for 400-20 from both the ordered structure of  $\gamma'_N/\gamma''_N$  (retained from the pre-existing  $\gamma'/\gamma''$  intermetallic precipitates at low treatment temperature) and the N short-range ordering in  $\gamma_N$ . In this case, the total absence of superlattice reflections on 400-20 appears rather intriguing and may benefit from further attention. One might anticipate that N short-range ordering (e.g. at body centres) occurs in the FCC- $\gamma_N$  matrix (and perhaps in  $\gamma''_N$ ) on 400-20 but causes destructive interference to (subtracting, instead of intensifying) the superlattice diffraction from the ordered structure of  $\gamma'_N/\gamma''_N$ , considering the  $\sim 600$  nm diameter diffraction aperture used in this study (that selects  $\gamma_N$ ,  $\gamma'_N$  and  $\gamma''_N$  collectively). Nevertheless, this supposition is still to be confirmed by further crystallographic analysis (of  $\gamma_N/\gamma'_N/\gamma''_N$  separately, if possible) in combination with modelling/simulation.

### 3.3. Surface nitrogen modification

The surface nitrogen content in Table 2 was evaluated using SEM-EDX with respect to the main alloying elements, i.e. Ni, Fe, Cr, Nb, Mo, Ti, Al, Cu and Si. Firstly, the surface nitrogen content for 400 °C and 20 h TPN-treated alloy 718 is found to be  $\sim 23$  at.%, a value that appears somewhat lower than those expected of ASSs (i.e.  $\sim 27$  at.% N for AISI 304,  $\sim 34$  at.% N for high-Mn alloy AG17 and  $\sim 24$  at.% for high-Ni alloy 330 [53]) under equivalent treatment conditions. The slightly lower

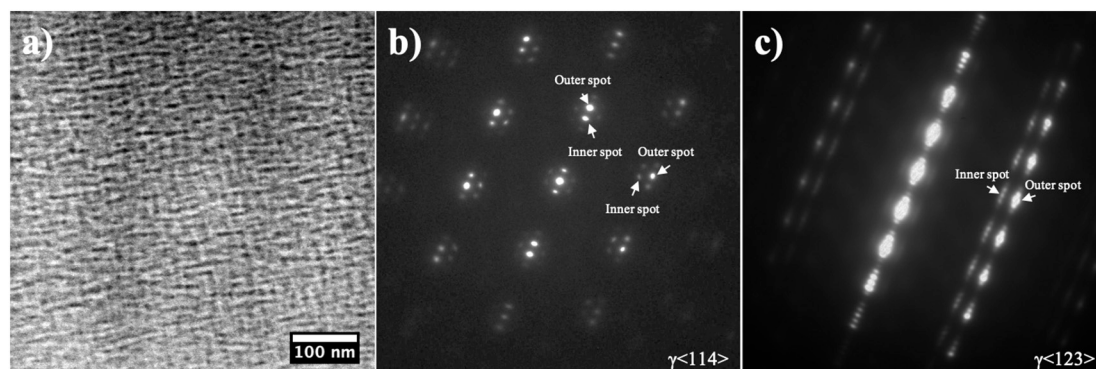
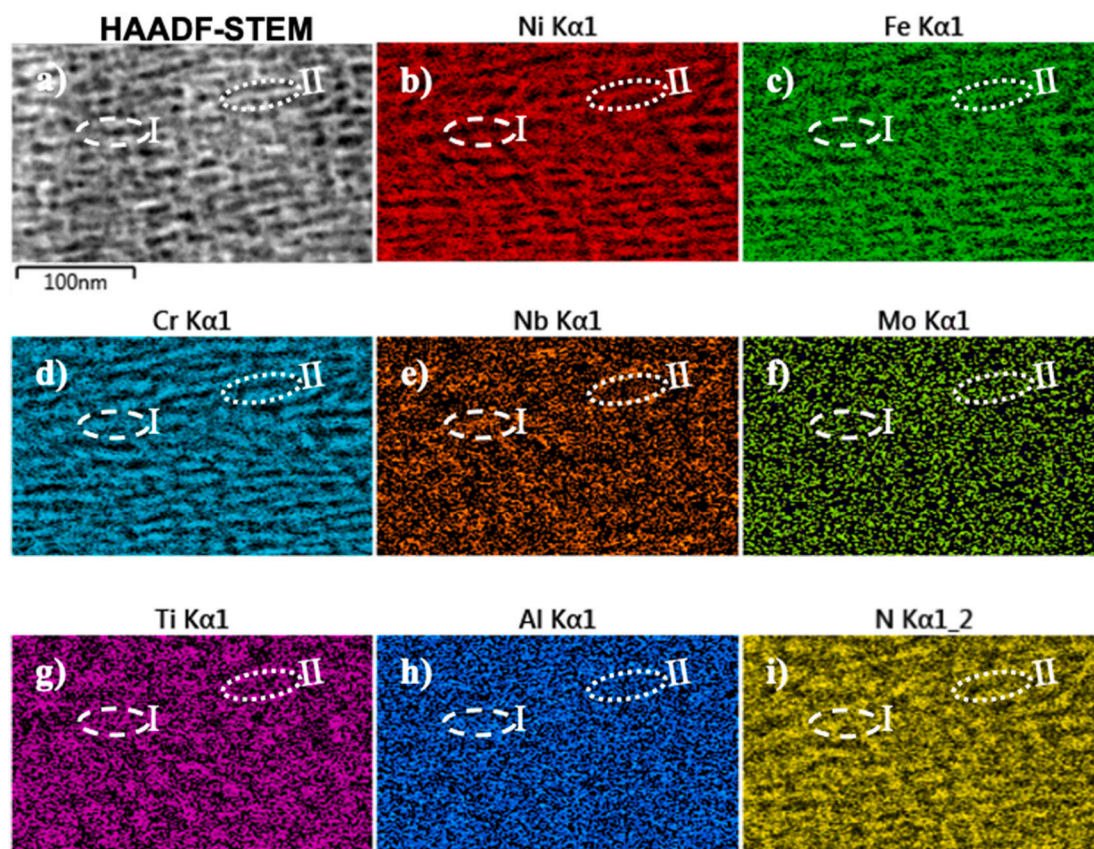


Fig. 7. a) STEM-HAADF image for the topmost treatment layer on 700-1 (taken at depth  $< 1 \mu\text{m}$ ) and b, c) corresponding EDPs.



**Fig. 8.** STEM-EDX analysis for the topmost surface (images taken at depth  $< 1 \mu\text{m}$ ) on 700-1, a) HAADF-STEM image, b) corresponding EDX maps for b) Ni, c) Fe, d) Cr, e) Nb, f) Mo, g) Ti, h) Al, and i) N. Two regions were highlighted by circles to guide viewing. Note that element maps in Fig. 8b–i do not perfectly superimpose with Fig. 8a owing to sample drift during prolonged EDX elemental scan.

surface nitrogen content of alloy 718 after TPN at  $400^\circ\text{C}$  is attributable to a Ni-based matrix. The  $\gamma_{\text{N}}$  matrix and  $\gamma''_{\text{N}}$  are thought to have higher nitrogen content than the ‘overall’  $\sim 23$  at.% measured on 400-20, considering the large volume of “slightly-expanded” Al-rich  $\gamma'_{\text{N}}$  which presumably possess very low nitrogen absorption. Secondly, comparing the nitrogen content to those found after TPN under thermodynamic paraequilibrium at  $400\text{--}450^\circ\text{C}$ , rather low surface nitrogen contents

were measured at  $\sim 14\text{--}16$  at.% for treatment at  $700^\circ\text{C}$ , under thermodynamic equilibrium (Table 2), suggesting relatively low surface nitrogen solvency at the higher temperature. However, it can be argued that treatment times of 1 h and 4 h are too short to build up a high surface N content on 700-1/700-4, based on an expected substantially higher nitrogen inward diffusion rate at a higher temperature. The low surface nitrogen content at  $700^\circ\text{C}$  can also be caused by the intensified

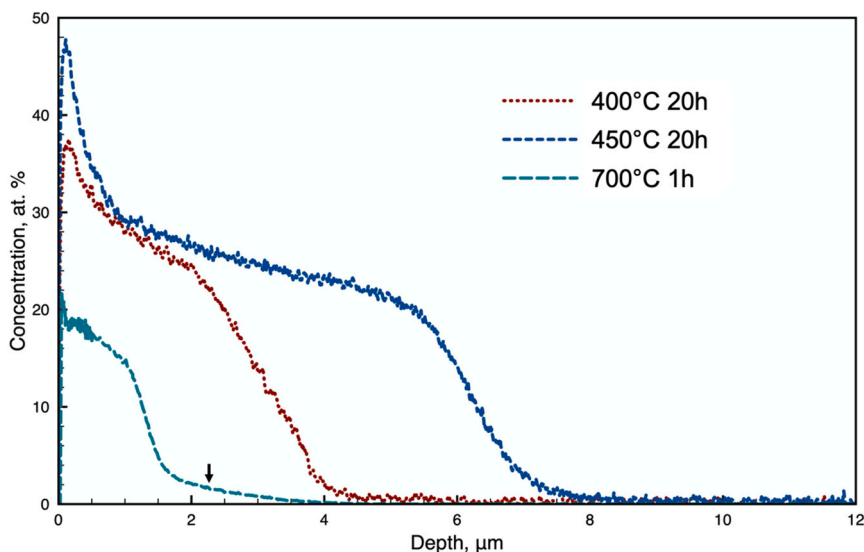


**Fig. 9.** GDOES nitrogen depth profile for alloy 718 after TPN treatment at  $400^\circ\text{C}$  for 20 h, at  $450^\circ\text{C}$  for 20 h and at  $700^\circ\text{C}$  for 1 h. A rather long N “tail” is indicated by arrow for the sample treated at  $700^\circ\text{C}$  for 1 h, suggesting a low-N diffusion zone.

plasma heating and the strong sputter removal effect. Noticeably, the SEM-EDX (20 keV) interaction depth should be typically <1 μm (estimated from substrate chemical composition, using Monte Carlo simulation by CASINO software). While the surface nitrogen contents at 400–450 °C (Table 2) should entirely originate from the treatment layer, the measured values for 700 °C TPN-treated surfaces might be partly contributed to by the (low-N) regions below the thin treatment layers.

Nitrogen depth profiles for 400-20 and 450-20 in Fig. 9 show a 'plateau' with nitrogen concentration ranging from ~24 to 30 at.% and ~22 to 28 at.%, respectively. A nitrogen 'plateau' was also seen for 700-1 at a much lower nitrogen level of ~14–18 at.%, that is consistent with the low surface nitrogen content measured from SEM-EDX in Table 2. Interestingly, a ~2 μm deep tail was seen (below the high-N topmost layer) for 700-1 that shows low nitrogen content and a gradually reducing nitrogen profile (as indicated by the arrow in Fig. 9), indicating an underlying nitrogen diffusion zone. Nitrogen diffusion depth at 700 °C (e.g. ~4 μm for 700-1 as revealed in Fig. 9) appears to be much deeper than the layer thickness observed under BS-SEM alone. The absence of this underlying diffusion zone in Fig. 2e & f & i at 700 °C is apparently caused by its low nitrogen content and the less-pronounced influence on corrosion resistance to the etchant.

### 3.4. Surface hardening

Vickers hardness measurement was carried out on top of the TPN-treated surfaces on 400-20, 450-20 and 700-4 at indentation loads of 0.01–1 kg. No reliable hardness data were obtained on 700-4 at an indentation load of 0.01 kg, owing to its high surface roughness (as shown in Fig. 1). The surface hardness values were plotted against indentation load (Fig. 10a). Firstly, while different levels of surface hardening were obtained after TPN treatments, the core hardness remained unchanged at the selected low treatment temperatures (and/or short treatment times) in this study. Compared to the untreated Inconel 718 at 490 ± 29 HV<sub>0.025</sub> (as measured on top of the polished sample plate), the core hardness values for 400-20, 450-20 and 700-4 (as measured on the prepared sample cross-sections) are all comparable, at 497 ± 22 HV<sub>0.025</sub>, 492 ± 24 HV<sub>0.025</sub> and 486 ± 23, respectively. Then, it is noted that the treatment layers obtained are rather thin at the selected treatment conditions and that the treatment parameters (e.g., treatment pressure, workpiece current density, treatment temperature/time) can/should be optimised for obtaining thick treatment layers in the future studies. With increases in indentation depth, the contribution from the substrate increases and the measured surface hardness reduces, approaching the substrate hardness value. With regard to indentation depths, layer thicknesses (i.e. 4, 7, and 1.5 μm on 400-20, 450-20 and

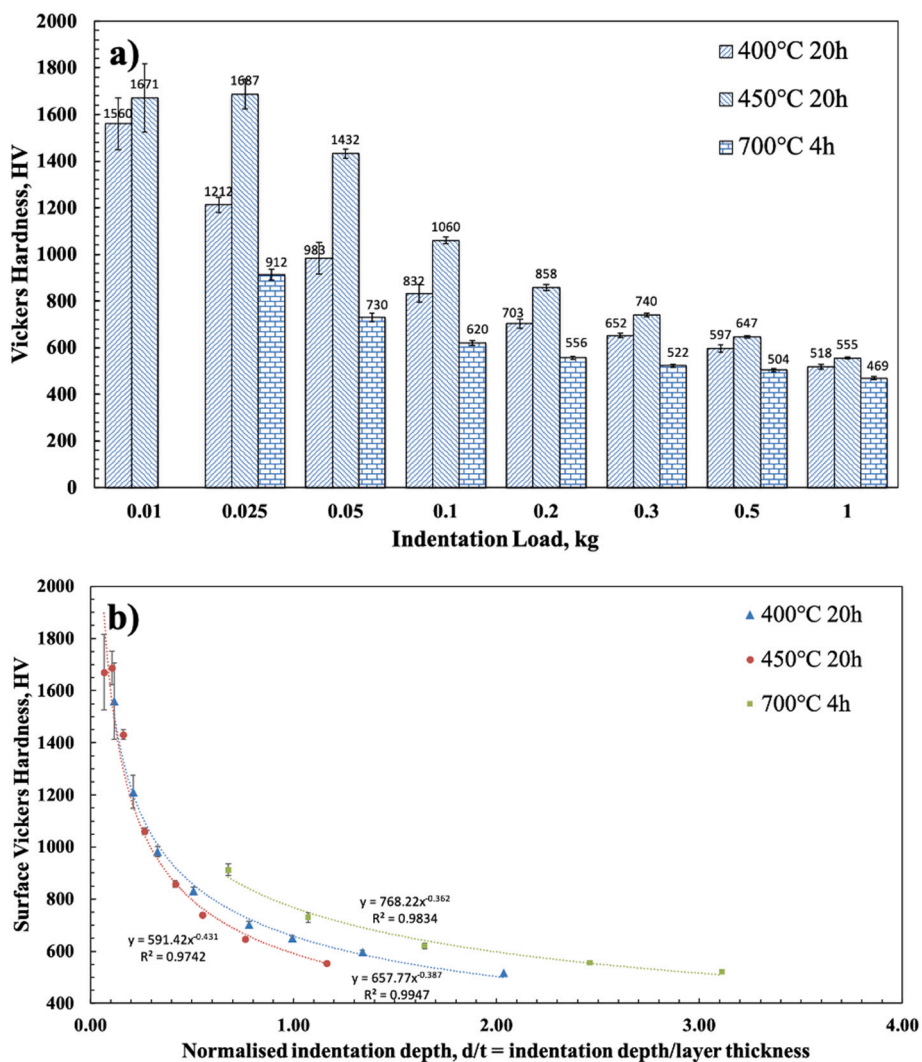


Fig. 10. Surface Vickers hardness of alloy 718 after TPN treatment at 400 °C for 20 h, at 450 °C for 20 h and at 700 °C for 4 h under different indentation loads (i.e. 0.01, 0.025, 0.05, 0.1, 0.2, 0.3, 0.5 and 1 kg). a) bar chart for hardness against indentation load and b) plot for the measured hardness value against normalised indentation depth (d/t = indentation depth/layer thickness).



700-4, respectively), and the “Bückle rule”, most surface hardness values in Fig. 10 do not represent the true “substrate-free” hardness of the treatment layers.

Nevertheless, the measured hardness can be plotted against normalised indentation depth ( $d/t = \text{indentation depth}/\text{layer thickness}$ ) in Fig. 10b, where the layer thicknesses for 400-20, 450-20 and 700-4 were taken as 4.2, 7.1, and 1.5  $\mu\text{m}$  (Table 2), respectively. For 450-20, the normalised indentation depths are 0.07 and 0.11 at indentation loads of 0.01 kg and 0.025 kg, respectively. At  $d/t$  values near 0.1 in Fig. 10b, the similar surface hardness values of 1671  $\text{HV}_{0.01}$  and 1687  $\text{HV}_{0.025}$  for 450-20 represent something close to the ‘true’ hardness of the treatment layer, which showed a dotted nitride precipitation morphology (Fig. 6b). Such hardness value for the treatment layer on 450-20 agrees well with those of  $\sim 1750\text{--}1850 \text{HV}_{0.05}$  for the thick layers (i.e. 13 and 16  $\mu\text{m}$  at 450 and 475  $^{\circ}\text{C}$  for 16 h, respectively) obtained on Inconel 718 after salt bath nitriding (which showed weak CrN XRD peaks) [23].

In addition, at the indentation load of 0.01 kg, the measured surface hardness value for 400-20 at  $\sim 1560 \text{HV}_{0.01}$  is only slightly lower than the hardness for 450-20 at  $\sim 1671 \text{HV}_{0.01}$ . The nitrogen interstitial-supersaturated layer on 400-20 also possesses high hardness, close to that for the treatment layer on 450-20 (typically when approaching  $d/t \sim 0.1$  in Fig. 10b). The early-stage nitride formation in the treatment layer on 450-20 does not seem to significantly increase the hardness of the treatment layer. Nevertheless, it was shown that substantial nitride formation in the treatment layer on plasma nitrided Inconel 718 can lead to a further increase in surface hardness [28]. Accompanied with strong CrN XRD peaks, a high surface hardness of  $\sim 2100 \text{HV}_{0.05}$  was reported for the  $\sim 25 \mu\text{m}$  thick treatment layer obtained after salt bath nitriding at 500  $^{\circ}\text{C}$  for 16 h [23]. At a given  $d/t$  within the nitrided layer (i.e.  $d/t < 1$ ) in Fig. 10b, the hardness value for 700-4 is significantly higher than those for 400-20 and 450-20, indicating an improved hardness for the nitrided layer on 700-4. The low hardness values measured on 700-4 in this study (which should show a woven nitride precipitation morphology with significant Cr-segregation, Section 3.2) are believed to occur primarily as a consequence of the low layer thickness.

### 3.5. Corrosion performance

After TPN treatment at 400  $^{\circ}\text{C}$  for 20 h, the potentiodynamic polarization curve is shifted upward to a more noble position after nitrogen supersaturation (Fig. 11), which correlates well to the increased open circuit potential in 0.1 N NaCl aqueous solution for annealed Inconel

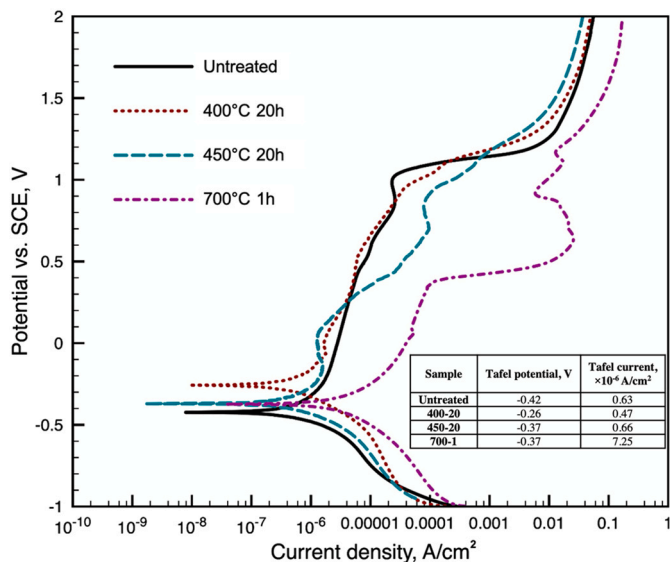


Fig. 11. Potentiodynamic polarization curves for alloy 718 before and after TPN treatment at 400  $^{\circ}\text{C}$  for 20 h, at 450  $^{\circ}\text{C}$  for 20 h and at 700  $^{\circ}\text{C}$  for 1 h.

718 after low-temperature plasma nitriding [20]. No signs of degradation in corrosion performance were seen for 400-20 over the untreated substrate. This is also found to be consistent with the preserved corrosion performance of nitrogen-supersaturated layers of  $\gamma_{\text{N}}$  obtained on austenitic stainless steels after low-temperature plasma nitriding treatments [53,59]. For the nitrogen-supersaturated layer obtained in the 400-20 TPN treatment of Inconel 718, the different nitriding responses between phases (i.e. the  $\gamma'/\gamma''$  nanoprecipitates and the  $\gamma$  matrix) do not appear to influence the preservation of corrosion performance, which can be understood by the absence of long-range elemental migration of substitutional atoms (such as Fe, Cr, Ni, etc.) at the low treatment temperature.

Although slight increases in corrosion current density can be seen in the anodic region at  $\sim +0.3$  to  $+1.1 \text{V}$  on 450-20, the dotted nitride precipitation at 450  $^{\circ}\text{C}$  for 20 h is still insufficient to cause substantial influence to corrosion performance. It appears that early-stage nitride formation on Inconel 718 does not necessarily result in deteriorated corrosion performance. Nevertheless, a substantial loss in corrosion performance does become evident when pronounced nitride precipitation occurs, after TPN at a higher treatment temperature of 700  $^{\circ}\text{C}$ , since the potentiodynamic curve is shifted to the right (towards higher corrosion current densities). A similar shift in potentiodynamic curve and loss in corrosion performance was also reported for Inconel 718 (with CrN formation) after plasma nitriding at 500  $^{\circ}\text{C}$  for 6 h [28]. Additionally, compared to the broad passivation region for untreated alloy 718 until  $\sim +1.0 \text{V}$ , the passive region on 700-1 extends to only  $\sim +0.4 \text{V}$ , indicating reduced passivity. As has been demonstrated for the decomposition of  $\gamma_{\text{N}}$  layers on austenitic stainless steels [53,59], such deteriorated corrosion performance of 700-4 is attributable to the significant elemental segregation (of Cr, Ti, Nb, etc.) and large volumes of Cr-depleted regions at 700  $^{\circ}\text{C}$  (Fig. 8).

## 4. Conclusions

This study investigates a precipitation-strengthened Ni-superalloy, Inconel 718, after TPN treatments at 400–450  $^{\circ}\text{C}$  for 4 h and 20 h and at 700  $^{\circ}\text{C}$  for 1–4 h, respectively. Conclusions can be drawn as below:

- After TPN treatment at 400  $^{\circ}\text{C}$  for 20 h, significant XRD peak shifting was observed, which is characteristic of the formation of nitrogen-expanded austenite and corresponds to the anisotropic expansion of the  $\gamma$ -FCC matrix under nitrogen interstitial supersaturation.
- More importantly, in contrast to  $\gamma_{\text{N}}$  layers typically synthesised on ASSs, the nitrogen-supersaturated layer on precipitation strengthened alloy 718 contains  $\gamma'_{\text{N}}$  and  $\gamma''_{\text{N}}$ , owing to nitrogen modification of the pre-existing precipitation-strengthening  $\gamma'$  and  $\gamma''$  phases. A slightly expanded phase can be identified, corresponding to  $\sim 5\text{--}20 \text{nm}$  diameter spheroidal  $\text{Ni}_3\text{Al}$ -type  $\gamma'_{\text{N}}$ . On the other hand,  $\gamma''_{\text{N}}$  was not directly observed, but  $\gamma''_{\text{N}}$  may have expanded lattice parameters close to that of  $\gamma_{\text{N}}$  matrix, such that no additional peak was seen under (GA)XRD and no extra diffraction spots were observed in EDP.
- After TPN at 450  $^{\circ}\text{C}$  and 20 h, finely dispersed nitride “dots” of  $\sim 3\text{--}6 \text{nm}$  diameter were revealed, following a cube-on-cube orientation relationship to the FCC matrix, i.e.  $\langle 111 \rangle_{\text{nitride}} // \langle 111 \rangle_{\gamma}$  and  $\{110\}_{\text{nitride}} // \{110\}_{\gamma}$ .
- Approaching thermodynamic equilibrium at a high treatment temperature of 700  $^{\circ}\text{C}$ , a “woven” morphology was observed with nitride formation, where STEM-EDX analysis suggests pronounced migration of Cr and N towards (and rejection of Fe and Ni from) nitride precipitate regions in the topmost layer of the 700  $^{\circ}\text{C}$  TPN-treated surface.
- For the nitride formed on alloy 718 after TPN at 700  $^{\circ}\text{C}$ , the elemental distributions of Ti and Nb also correlate closely to those of Cr and N, suggesting that CrN could contain Ti and Nb. Al and Mo present a more homogenous distribution, but it cannot be stated unequivocally that CrN contains Al and Mo (at all – or in quantities

higher than the surrounding matrix), because of their low overall concentration. The precise composition of nitrides would still require further investigation using advanced characterisation techniques, such as Atom Probe Tomography.

- Substantial nitrogen absorption and surface hardening were achieved for all TPN-treated samples, while no significant change in microstructure/property is expected for the material core at the selected treatment conditions. Surface hardness was increased from ~480 HV (before TPN treatment) to 1560 HV<sub>0.01</sub> and 1671 HV<sub>0.01</sub> after TPN at 400 °C for 20 h and 450 °C for 20 h, respectively. The rather low surface hardness (at ~912 HV<sub>0.025</sub>) for 700-4 is attributed to the thin treatment layer, with a significant substrate contribution to the measured values.
- While no loss in corrosion performance was seen for the nitrogen-supersaturated layer after TPN at 400 °C, the early-stage nitride formation for 450-20 shows slightly increased current densities in the anodic polarization region. The significantly deteriorated

corrosion performance at an elevated treatment temperature of 700 °C correlates well to the pronounced nitride precipitation and could be attributed to local Cr-depletion.

#### Declaration of competing interest

The authors declare that they have no known competing financial interests or personal relationships that could have appeared to influence the work reported in this paper.

#### Acknowledgements

We acknowledge the support provided by Dr. Peng Zeng and Dr. Le Ma from the Sorby Centre for Electron Microscopy at the University of Sheffield and by Mr. Paul Stanley from the Centre for Electron Microscopy at the University of Birmingham.

## Appendix A

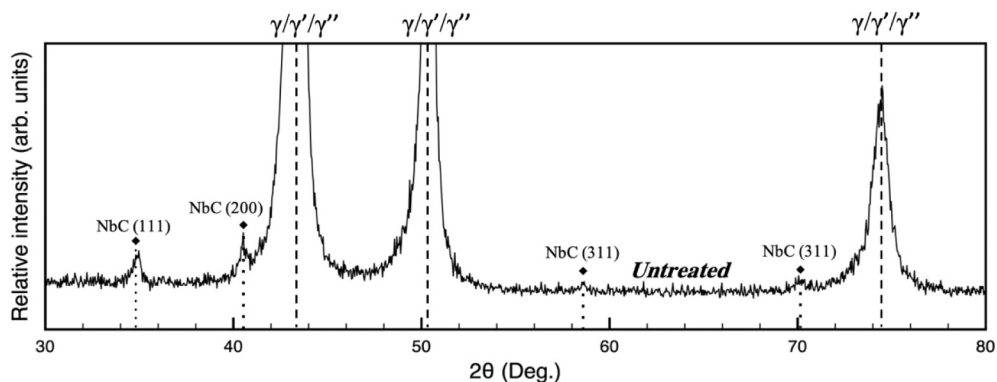


Fig. A1. GAXRD profile for Inconel 718 before TPN treatment (i.e. the same data, but magnified, to that presented in Fig. 3b), showing the pre-existing NbC.

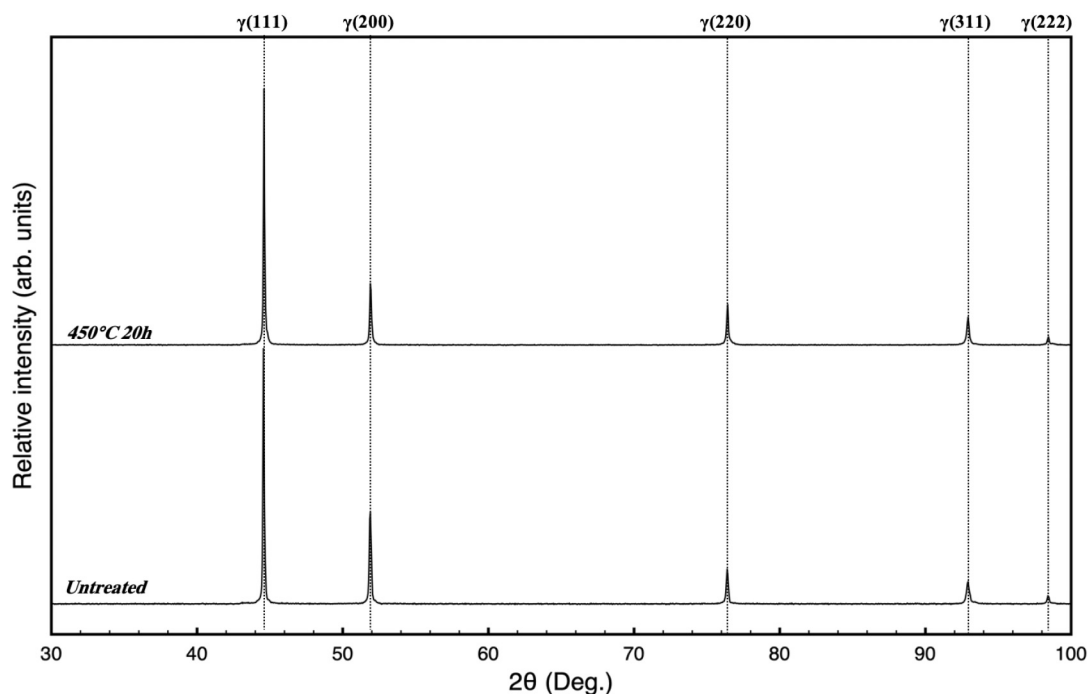


Fig. A2. XRD profiles for commercial pure Ni, VDM® 201, before and after TPN treatment at 450 °C for 20 h, showing no signs of peak shifting nor nitride formation. XRD profiles were taken under Bragg-Brentano geometry using a Bruker D2 PHASER (30 kV, 10 mA; Cu-K<sub>α</sub> 0.1542 nm) as described in Experimental. X-ray K<sub>α</sub> signals were removed.

## References

- [1] S.P. Hannula, O. Nenonen, J.-P. Hirvonen, Surface structure and properties of ion-nitrided austenitic stainless steels, *Thin Solid Films* 181 (1989) 343–350.
- [2] D.L. Williamson, L. Wang, R. Wei, P.J. Wilbur, Solid solution strengthening of stainless steel surface layers by rapid, high dose, elevated temperature nitrogen ion implantation, *Mater. Lett.* 9 (1990) 302–308.
- [3] A. Leyland, D.B. Lewis, P.R. Stevenson, A. Matthews, Low temperature plasma diffusion treatment of stainless steels for improved wear resistance, *Surf. Coat. Technol.* 62 (1993) 608–617.
- [4] T. Christiansen, M.A.J. Somers, On the crystallographic structure of S-phase, *Scr. Mater.* 50 (2004) 35–37.
- [5] Z.L. Zhang, T. Bell, Structure and corrosion resistance of plasma nitrided stainless steel, *Surf. Eng.* 1 (1985) 131–136.
- [6] K. Ichii, K. Fujimura, T. Takase, Structure of the ion-nitrided layer of 18-8 stainless steel, *Technol. Rep. Kansai Univ.* 27 (1986) 135–144.
- [7] Y. Sun, X.Y. Li, T. Bell, X-ray diffraction characterisation of low temperature plasma nitrided austenitic stainless steels, *J. Mater. Sci.* 34 (1999) 4793–4802.
- [8] H. Dong, S-phase surface engineering of Fe-Cr, Co-Cr and Ni-Cr alloys, *Int. Mater. Rev.* 55 (2010) 65–98.
- [9] D.L. Williamson, O. Ozturk, Metastable phase formation and enhanced diffusion in f.c.c. alloys under high dose, high flux nitrogen implantation at high and low ion energies, *Surf. Coat. Technol.* 65 (1994) 15–23.
- [10] H.L. Eiselstein, Metallurgy of a Columbium-Hardened Nickel-Chromium-Iron Alloy, ASTM International, West Conshohocken, PA, 1965, pp. 62–79.
- [11] J. Kolts, Alloy 718 for the oil and gas industry, in: E.A. Loria (Ed.), *Superalloy 718—Metallurgy and Applications*, TMS, Warrendale, PA, 1989, pp. 329–344.
- [12] O.A. Onyewuanyi, Alloy 718 - alloy optimization for applications in oil and gas production, in: E.A. Loria (Ed.), *Superalloy 718—Metallurgy and Applications*, TMS, Warrendale, PA, 1989, pp. 345–362.
- [13] E.A. Loria, M. Minerals, M. Society, A. International, N.A.o.C. Engineers, N.D. Institute, Superalloys 718, 625, 706 and various derivatives: proceedings of the international symposium on superalloys 718, 625, 706 and various derivatives, in: *The Society*, 1997.
- [14] J.J. deBarbadillo, S.K. Mannan, Alloy 718 for oilfield applications, *JOM* 64 (2012) 265–270.
- [15] R. Cozar, A. Pineau, Morphology of  $\gamma'$  and  $\gamma''$  precipitates and thermal stability of inconel 718 type alloys, *Metall. Trans.* 4 (1973) 47–59.
- [16] D.D. Keiser, H.L. Brown, Review of the Physical Metallurgy of Alloy 718, 1976. <https://www.osti.gov/biblio/4016087>.
- [17] C. Slama, M. Abdellaoui, Structural characterization of the aged Inconel 718, *J. Alloys Compd.* 306 (2000) 277–284.
- [18] R. Lawitzki, S. Hassan, L. Karge, J. Wagner, D. Wang, J. von Kobylinski, C. Kremaszky, M. Hofmann, R. Gilles, G. Schmitz, Differentiation of  $\gamma'$ - and  $\gamma''$ -precipitates in Inconel 718 by a complementary study with small-angle neutron scattering and analytical microscopy, *Acta Mater.* 163 (2019) 28–39.
- [19] P.K. Aw, A.W. Batchelor, N.L. Loh, Structure and tribological properties of plasma nitrided surface films on Inconel 718, *Surf. Coat. Technol.* 89 (1997) 70–76.
- [20] V. Singh, E.I. Meletis, Synthesis, characterization and properties of intensified plasma-assisted nitrided superalloy Inconel 718, *Surf. Coat. Technol.* 201 (2006) 1093–1101.
- [21] A. Houghton, R. Lewis, U. Olofsson, J. Sundh, Characterising and reducing seizure wear of inconel and incoloy superalloys in a sliding contact, *Wear* 271 (2011) 1671–1680.
- [22] S. Chollet, L. Pichon, J. Cormier, J.B. Dubois, P. Villechaise, M. Drouet, A. Declémy, C. Templier, Plasma assisted nitriding of Ni-based superalloys with various microstructures, *Surf. Coat. Technol.* 235 (2013) 318–325.
- [23] Y. Jing, W. Jun, G. Tan, X. Ji, F. Hongyuan, Phase transformations during low temperature nitrided Inconel 718 superalloy, *ISIJ Int.* 56 (2016) 1076–1082.
- [24] H. Kováč, H. Ghahramanzadeh Asl, Ç. Albayrak, A. Alsaran, A. Çelik, Effect of plasma nitriding parameters on the wear resistance of alloy Inconel 718, *Met. Sci. Heat Treat.* 58 (2016) 470–474.
- [25] H. Zhang, H. Qin, Z. Ren, J. Zhao, X. Hou, G.L. Doll, Y. Dong, C. Ye, Low-temperature nitriding of nanocrystalline Inconel 718 alloy, *Surf. Coat. Technol.* 330 (2017) 10–16.
- [26] G.C. Mondragón-Rodríguez, N. Torres-Padilla, N. Camacho, D.G. Espinosa-Arbeláez, G.V. de León-Nope, J.M. González-Carmona, J.M. Alvarado-Orozco, Surface modification and tribological behavior of plasma nitrided Inconel 718 manufactured via direct melting laser sintering method, *Surf. Coat. Technol.* 387 (2020), 125526.
- [27] L. Xue, J. Wang, L. Li, G. Chen, L. Sun, S. Yu, Enhancement of wear and erosion-corrosion resistance of Inconel 718 alloy by liquid nitriding, *Mater. Res. Express* 7 (2020), 096510.
- [28] A. Maniee, F. Mahboubi, R. Soleimani, Improved hardness, wear and corrosion resistance of Inconel 718 treated by hot wall plasma nitriding, *Met. Mater. Int.* 26 (2020) 1664–1670.
- [29] D.L. Williamson, I. Ivanov, R. Wei, P.J. Wilbur, Role of chromium in high-dose, high rate, elevated temperature nitrogen implantation of austenitic stainless steels, *Mater. Res. Soc. Symp. Proc.* 235 (1992).
- [30] X. Tao, A. Matthews, A. Leyland, On the nitrogen-induced lattice expansion of a non-stainless austenitic steel, Invar 36®, under triode plasma nitriding, *Metall. Mater. Trans. A* 51 (2020) 436–447.
- [31] T. Makishi, K. Nakata, Surface hardening of nickel alloys by means of plasma nitriding, *Metall. Mater. Trans. A* 35A (2004) 227–238.
- [32] L. Pichon, J. Cormier, A. Declémy, S. Chollet, P. Villechaise, J.B. Dubois, C. Templier, Plasma nitriding response at 400 °C of the single crystalline Ni-based superalloy MC2, *J. Mater. Sci.* 48 (2013) 1585–1592.
- [33] L. Pichon, J.-B. Dubois, S. Chollet, F. Larek, J. Cormier, C. Templier, Low temperature nitriding behaviour of Ni3Al-like  $\gamma'$  precipitates in nickel-based superalloys, *J. Alloys Compd.* 771 (2019) 176–186.
- [34] A. Leyland, K.S. Fancey, A.S. James, A. Matthews, Enhanced plasma nitriding at low pressures: a comparative study of d.c. and r.f. techniques, *Surf. Coat. Technol.* 41 (1990) 295–304.
- [35] A. Leyland, K.S. Fancey, A. Matthews, Plasma nitriding in a low pressure triode discharge to provide improvements in adhesion and load support for wear resistant coatings, *Surf. Eng.* 7 (1991) 207–215.
- [36] X. Tao, Investigations on the Role of Cr, Mn and Ni on the Formation, Structure, and Metastability of Nitrogen-Expanded Austenite on Fe-based Austenitic Alloys under Triode-plasma Nitriding (PhD Thesis), Department of Materials Science and Engineering, University of Sheffield, 2018.
- [37] X. Tao, X. Liu, A. Matthews, A. Leyland, The influence of stacking fault energy on plasticity mechanisms in triode-plasma nitrided austenitic stainless steels: implications for the structure and stability of nitrogen-expanded austenite, *Acta Mater.* 164 (2019) 60–75.
- [38] G. Cassar, Improvement in Tribological Characteristics of Titanium Alloys Using Duplex Intensified Plasma Treatment (PhD Thesis), Department of Materials Science and Engineering University of Sheffield, 2011.
- [39] G. Cassar, S. Banfield, J.C.A.-B. Wilson, J. Housden, A. Matthews, A. Leyland, Tribological properties of duplex plasma oxidised, nitrided and PVD coated Ti-6Al-4V, *Surf. Coat. Technol.* 206 (2011) 395–404.
- [40] G. Cassar, A. Matthews, A. Leyland, Triode plasma diffusion treatment of titanium alloys, *Surf. Coat. Technol.* 212 (2012) 20–31.
- [41] G. Cassar, S. Banfield, J.C. Avelar-Batista Wilson, J. Housden, A. Matthews, A. Leyland, Micro-abrasion wear testing of triode plasma diffusion and duplex treated Ti-6Al-4V, *Wear* 274-275 (2012) 377–387.
- [42] G. Cassar, S. Banfield, J.C. Avelar-Batista Wilson, J. Housden, A. Matthews, A. Leyland, Impact wear resistance of plasma diffusion treated and duplex treated/PVD-coated Ti-6Al-4V alloy, *Surf. Coat. Technol.* 206 (2012) 2645–2654.
- [43] K.S. Fancey, A. Matthews, Some fundamental aspects of glow discharges in plasma-assisted processes, *Surf. Coat. Technol.* 33 (1987) 17–29.
- [44] J.C. Stinville, C. Templier, P. Villechaise, L. Pichon, Swelling of 316L austenitic stainless steel induced by plasma nitriding, *J. Mater. Sci.* 46 (2011) 5503–5511.
- [45] K.S. Fancey, A. Matthews, Process effects in ion plating, *Vacuum* 41 (1990) 2196–2200.
- [46] K.M. Eliassen, T.L. Christiansen, M.A.J. Somers, Low temperature gaseous nitriding of Ni based superalloys, *Surf. Eng.* 26 (2010) 248–255.
- [47] Y. Sun, Kinetics of layer growth during plasma nitriding of nickel based alloy Inconel 600, *J. Alloys Compd.* 351 (2003) 241–247.
- [48] G. Yumusak, A. Leyland, A. Matthews, The effect of pre-deposited titanium-based PVD metallic thin films on the nitrogen diffusion efficiency and wear behaviour of nitrided Ti alloys, *Surf. Coat. Technol.* 394 (2020), 125545.
- [49] S.J. Hong, W.P. Chen, T.W. Wang, A diffraction study of the  $\gamma''$  phase in INCONEL 718 superalloy, *Metall. Mater. Trans. A* 32 (2001) 1887–1901.
- [50] B. Dubiel, A. Kruk, E. Stepniowska, G. Cempura, D. Geiger, P. Formanek, J. Hernandez, P. Midgley, A. Czyska-Filemonowicz, TEM, HRTEM, electron holography and electron tomography studies of gamma' and gamma'' nanoparticles in Inconel 718 superalloy, *J. Microsc.* 236 (2009) 149–157.
- [51] D.L. Williamson, J.A. Davis, P.J. Wilbur, Effect of austenitic stainless steel composition on low-energy, high-flux nitrogen ion beam processing, *Surf. Coat. Technol.* 103-104 (1998) 178–184.
- [52] X. Tao, J. Qi, M. Rainforth, A. Matthews, A. Leyland, On the interstitial induced lattice inhomogeneities in nitrogen-expanded austenite, *Scr. Mater.* 185 (2020) 146–151.
- [53] X. Tao, X. Li, H. Dong, A. Matthews, A. Leyland, Evaluation of the sliding wear and corrosion performance of triode-plasma nitrided Fe-17Cr-20Mn-0.5N high-manganese and Fe-19Cr-35Ni-1.2Si high-nickel austenitic stainless steels, *Surf. Coat. Technol.* 409 (2021), 126890.
- [54] M. Kusunoki, S. Nagakura, Modulated structure of iron-carbon martensite studied by electron microscopy and diffraction, *J. Appl. Crystallogr.* 14 (1981) 329–336.
- [55] B.K. Brink, K. Stahl, T. Christiansen, C. Frandsen, M.F. Hansen, M.A.J. Somers, Composition-dependent variation of magnetic properties and interstitial ordering in homogenous expanded austenite, *Acta Mater.* 106 (2016) 32–39.
- [56] H.L. Che, S. Tong, K.S. Wang, M.K. Lei, M.A.J. Somers, Co-existence of  $\gamma'$ N phase and  $\gamma$ N phase on nitrided austenitic Fe-Cr-Ni alloys – I. experiment, *Acta Mater.* 177 (2019) 35–45.
- [57] J.C. Jiang, E.I. Meletis, Microstructure of the nitride layer of AISI 316 stainless steel produced by intensified plasma assisted processing, *J. Appl. Phys.* 88 (2000) 4026–4031.
- [58] K. Tong, F. Ye, H. Che, M.K. Lei, S. Miao, C. Zhang, High-density stacking faults in a supersaturated nitrided layer on austenitic stainless steel, *J. Appl. Crystallogr.* 49 (2016) 1967–1971.
- [59] C.X. Li, T. Bell, Corrosion properties of active screen plasma nitrided 316 austenitic stainless steel, *Corros. Sci.* 46 (2004) 1527–1547.